ACS APPLIED NANO MATERIALS

www.acsanm.org Article

S-Scheme α-Fe_2O_3/g-C_3N_4 Nanocomposites as Heterojunction Photocatalysts for Antibiotic Degradation

Viet Van Pham, Thao Kim Truong, Le Viet Hai, Ha Phan Phuong La, Hoang Thai Nguyen, Vinh Quang Lam, Hien Duy Tong, Thang Quoc Nguyen, Amr Sabbah, Kuei-Hsien Chen, Sheng-Jie You, and Thi Minh Cao*

Cite This: https://doi.org/10.1021/acsanm.2c00741 Read Online

ABSTRACT: The residue of antibiotics in the water has led to increased antibiotic-resistant bacteria, harm to human health, and damage to health-beneficial healthy bacteria. An idea of constructing S-scheme α-Fe_2O_3/g-C_3N_4 nanocomposites is studied toward a photocatalysis application for an efficient resolution of commercial antibiotics in wastewater. Outstanding S-scheme Fe_2O_3/g-C_3N_4 nanocatalysts are synthesized by a straightforward method and could easily improve the recycling property, thanks to magnetic materials. Empirical results indicate that S-scheme Fe_2O_3/g-C_3N_4 photocatalysts can degrade commercial cefalexin and amoxicillin (20 mg L^{-1}) under visible light, with five and nine times higher performance than that of g-C_3N_4, respectively. Furthermore, the detailed evidence to propose S-scheme Fe_2O_3/g-C_3N_4 heterojunctions and comparison of photocatalytic performance in antibiotic degradation have also been mentioned in this study.

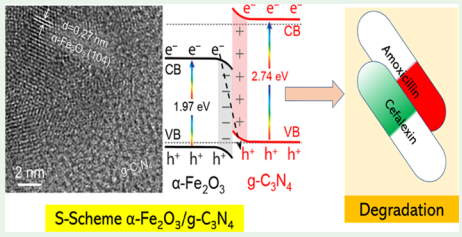

KEYWORDS: *α-Fe_2O_3, g-C_3N_4, photocatalysis, α-Fe_2O_3/g-C_3N_4, S-scheme, antibiotic degradation*

1. INTRODUCTION

Antibiotics such as cefalexin and amoxicillin have been extensively used for various disease treatments for humans and animals. However, these antibiotics are often incompletely metabolized, leading to significant excretion into the wastewater.[1,2] The long-term accumulation of these antibiotics can lead to severe consequences, for instance, the development of antibiotic-resistant bacteria, harm the human health, and damage the health-beneficial healthy bacteria.[3−6] Apparently, the conventional wastewater treatment approaches such as filtration, adsorption, and biodegradation cannot totally degrade the antibiotics because of their high stability and low biodegradability.[7,8]

Recently, nanomaterial-based semiconducting photocatalysis, which uses the endless solar energy source as input energy, is considered as an energy-effective, sustainable, environmentally friendly, and low-cost strategy for the degradation of organic pollutants.[9−11] In various semiconductor photocatalysts, graphite carbon nitride (g-C_3N_4) is considered one of the most potential candidates, owing to its unique properties such as high chemical and thermal stability and suitable band structure for the photooxidation applications.[12−16] However, the rapid recombination of photogenerated carriers and ineffective light utilization of g-C_3N_4 materials restricted their practical applications.[17−19] Recently, various efforts have been made, such as constructing heterojunctions, nanostructure design, doping with other elements, protonating with acid, and engineering nitrogen-deficiency defects.[17−20] Among them, the coupling of magnetic photocatalysts with g-C_3N_4 to form hybrid materials helps enable the material collection more easily utilizing a magnetic field.[19] As an expectation, α-Fe_2O_3, a semiconductor with a narrow band gap (2.0−2.2 eV), has prospective merits such as the most stable iron oxide, low corrosion, and accessible synthesis with low cost.[21,22] In addition, the narrow-band gap semiconductor of α-Fe_2O_3 harvests light effectively and expands the solar spectral response into the visible light region that constitutes 45−50% of the solar spectrum. Furthermore, α-Fe_2O_3 can contribute as active centers to improve the photocatalytic activity.[23] Consequently, α-Fe_2O_3-modified g-C_3N_4 is considered as a highlight approach to create low-cost, efficient, eco-friendly environmental photocatalysts. Many reports showed that composite materials of α-Fe_2O_3/g-C_3N_4 Z-scheme photocatalysts remarkably enhance the photocatalytic efficiency in water splitting for H_2 generation,[24−27] CO_2 reduction,[18,28−30] Cr(VI) and As removal,[31,32] organic dye degradation,[33−38] NO oxidation,[39] and so forth. In general, previous studies on Fe_2O_3/g-C_3N_4 nanocomposites indicated that combining these two materials created a Z-scheme photocatalyst, which led to superior charge transportation

Received: February 17, 2022
Accepted: February 25, 2022

and reduced recombination, leading to improved photocatalytic activity. However, a thorough understanding of the photocatalytic model of this material system is still a big challenge and needs to be investigated. Recently, Xu et al. proposed a direct Z-scheme charge transfer route with bending band energy edges of these two semiconductors, which can proceed over the Fe_2O_3/g-C_3N_4 composites, enhancing photocatalytic performance in H_2 generation.[24] This is considered as a premise for us to expand our survey and confirm the S-scheme photocatalyst model of α-Fe_2O_3/g-C_3N_4 heterojunctions. Moreover, the high photocatalytic degradation of commercial antibiotics (cefalexin and amoxicillin) with a high concentration in water is still a challenge, and developing S-scheme α-Fe_2O_3/g-C_3N_4 heterojunctions has high a scientific and practical value. In addition, the S-scheme photocatalyst model will be more helpful in understanding the separation and transformation of the charge carriers than the Z-scheme photocatalyst model. In detail, in the S-scheme model, we could easily understand the role of the internal electric field, band bending, and Coulombic attraction force, which contribute to the increase in the separation of electron–hole pairs in the α-Fe_2O_3 and g-C_3N_4 materials, leading to their enhanced photocatalytic ability.[16,40−42]

In this study, we synthesized α-Fe_2O_3-modified g-C_3N_4, with different α-Fe_2O_3 contents (as shown in Scheme 1) and investigated the photocatalytic degradation of antibiotics cefalexin and amoxicillin at high concentration for the purpose of understanding the photocatalytic activity of α-Fe_2O_3/g-C_3N_4 heterojunctions. The modification of g-C_3N_4 with α-Fe_2O_3 substantially improved the photocatalytic activity for high degradation of commercial cefalexin and amoxicillin (20 mg L^{-1}). The photocatalytic S-scheme mechanism of α-Fe_2O_3/g-C_3N_4 composites was confirmed from their considerably enhanced photocatalytic activity and the optical and electrochemical analyses. This study delivers a potential approach for pharmaceutical wastewater treatment employing direct S-scheme hybrid composite photocatalysts under visible light conditions.

Scheme 1. Synthesis Process of α-Fe_2O_3/g-C_3N_4 Nanocomposites

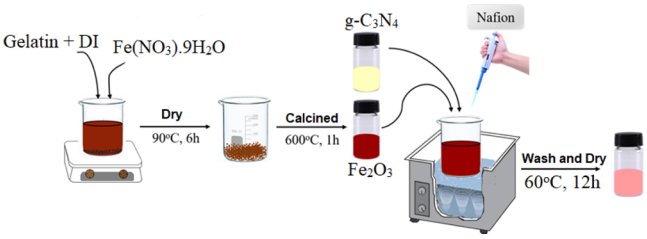

2. RESULTS AND DISCUSSION

2.1. Characterizations of α-Fe_2O_3/g-C_3N_4. The morphology and microstructure of the as-prepared catalysts were observed using HRTEM images and the selected-area electron diffraction (SAED) pattern (Figure 1). As could be observed in Figure 1a,b, g-C_3N_4 shows a lamellar structure, while α-Fe_2O_3 is in the form of nanoparticles with a diameter of 10 nm. The morphology of α-Fe_2O_3, g-C_3N_4, and 5% α-Fe_2O_3/g-C_3N_4 composites is also presented in SEM images (Figure S1). Furthermore, HRTEM images of the α-Fe_2O_3/g-C_3N_4 sample, verifying the good coupling between the two constituent materials via adhering together. From the HRTEM image (Figure 1c), an interplanar spacing of 0.27 nm, which corresponds to the (104) plane of α-Fe_2O_3,[26] is identified. Also, the diffraction rings in the SAED pattern (Figure 1d) of the composite could be indexed to the (104), (113), (1010), and (220) planes of α-Fe_2O_3 crystals. Moreover, as can be observed in the high-angle annular dark field-scanning transmission electron microscopy (HAADF-STEM) image (Figure 1e) and elemental mappings (Figure 1f–j), elements in g-C_3N_4 (C, N) and α-Fe_2O_3 (Fe, O) are uniformly distributed.

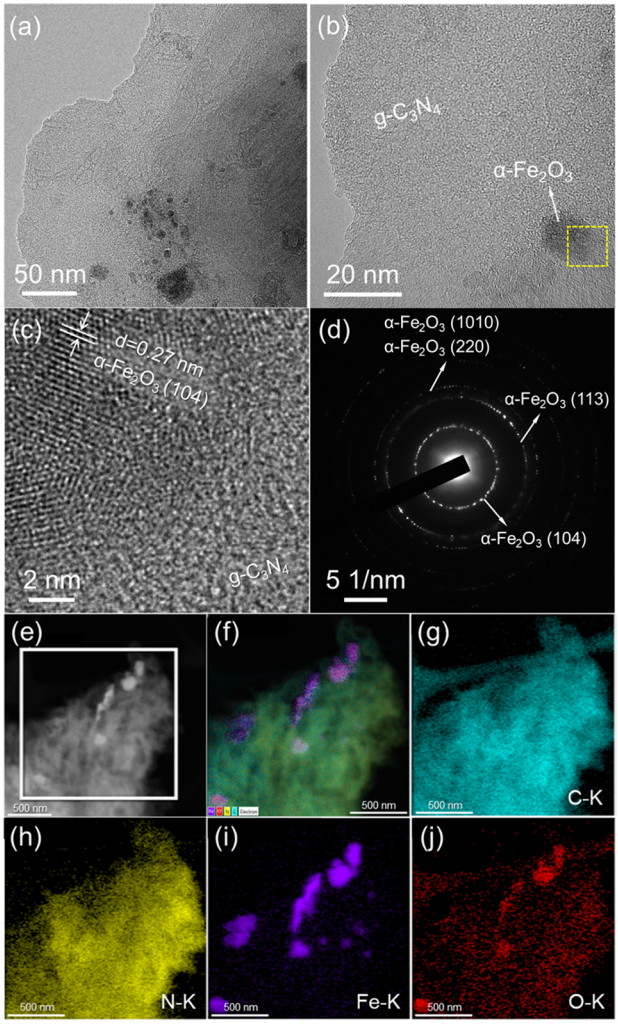

Figure 1. TEM images (a,b), HRTEM image (c), SAED pattern (d), HAADF-STEM image (e), and elemental mappings of α-Fe_2O_3/g-C_3N_4 (f–j).

Figure 2a presents XRD patterns of the as-synthesized α-Fe_2O_3, g-C_3N_4, and 5% α-Fe_2O_3 samples (which will be referred to as α-Fe_2O_3/g-C_3N_4 henceforth). For α-Fe_2O_3, the peaks located at 24.2, 33.1, 35.6, 40.9, 49.5, 54.1, 57.6, 62.5, 64.1, 71.9, and 75.5° are well-consistent with those of hematite (α-Fe_2O_3, JCPDS no. 33-0664) without the existence of a secondary phase. This result is so far well-consistent with SAED pattern results presented in Figure 1d. The g-C_3N_4 shows two characteristic peaks situated at 13.0° and 27.5°, corresponding to (100) and (002) planes of the g-C_3N_4 structure, respectively.[43] Furthermore, the peak belonging to the (100) plane of g-C_3N_4 suggests that the as-synthesized g-C_3N_4 is primarily made up of heptazine units rather than the s-

https://doi.org/10.1021/acsanm.2c00741
ACS Appl. Nano Mater. XXXX, XXX, XXX−XXX

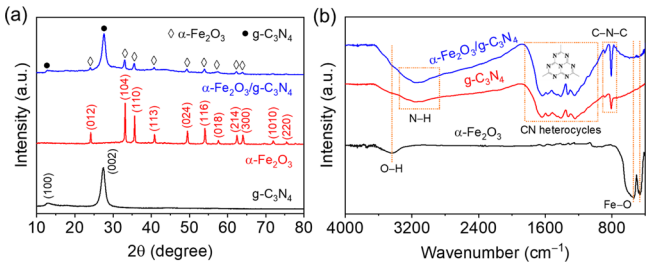

Figure 2. XRD patterns (a) and FTIR spectra (b) of α-Fe_2O_3, g-C_3N_4, and α-Fe_2O_3/g-C_3N_4.

triazine-based structure.[44] For the composite sample, the presence of characteristic diffraction peaks of both α-Fe_2O_3 and g-C_3N_4 is observed. Besides, the diffraction peak locations are not shifted, indicating unaffected crystal structures of α-Fe_2O_3 and g-C_3N_4 after composite construction.

The characteristic functional groups and bond vibrations of the as-prepared catalysts were investigated by FTIR spectroscopy (Figure 2b). The Fe_2O_3 presents two peaks at 469 and 542 cm^{-1}, which are assigned to Fe−O stretching modes.[45] The FTIR spectrum of g-C_3N_4 possesses three regions of typical vibrations. The first broad peak populated at 3000−3700 cm^{-1} is attributed to N−H and O−H stretching vibrations. The second region around 1210−1640 cm^{-1} is characteristic of C−N and C═N stretching modes of aromatic ring systems of the g-C3N4 principal structure.[46] The sharp peak at 810 cm^{-1} corresponds to the out-of-plane bending vibration belonging to heptazine rings.[47,48] For α-Fe_2O_3/g-C_3N_4, all typical vibration peaks of α-Fe_2O_3 and g-C_3N_4 concurrently exist, confirming the successful construction of the Fe_2O_3/g-C_3N_4 nanocomposite along with the above XRD results.

To further study the surface chemical composition and status of elements in the as-prepared materials, XPS survey spectrum analysis was carried out and is expressed in Figure S2. In detail, the XPS survey spectrum of g-C_3N_4 shows typical peaks of C 1s and N 1s, and Fe 2p and O 1s signals additionally appear in the XPS spectrum of the α-Fe_2O_3/g-C_3N_4 composite. For the C 1s region (Figure 3a), the XPS spectrum of g-C_3N_4 displays two major peaks at 284.8 and 288.1 eV, which are consistent with the C−C/C═C and N═C−N bonds, respectively.[26,48] The same result is observed in the XPS spectrum of α-Fe_2O_3/g-C_3N_4, where two peaks are fitted and located at 284.8 and 288.2 eV. However, the appearance of the C−O peak at around 285.9 eV in the composite spectrum is ascribed to carbon contamination. In the high-resolution spectra of N 1s exhibited in Figure 3b, the three peaks attributed to sp^2-hybridized nitrogen C═N−C, tertiary nitrogen N−$(C)_3$, and uncondensed terminal amino groups C−N−H are situated at 398.6, 400.0, and 401.1 eV, respectively, in g-C_3N_4.[49] For α-Fe_2O_3/g-C_3N_4, N−$(C)_3$ and C−N−H peaks shift slightly to the lower-binding energy region. In N 1s XPS spectra, the negative peak shift of α-Fe_2O_3/g-C_3N_4 compared to that of g-C_3N_4 reveals the formation of the composite structure. Moreover, due to the conjugated aromatic structure of g-C_3N_4, extended delocalized electrons could give rise to satellite signals (π−π^*) in higher-binding energy ranges of the main C 1s and N 1s peaks. As presented in Figure 3c, the O 1s XPS spectrum of g-C_3N_4 shows the main peak centered at 531.5 eV, which is ascribed to the surface hydroxyl groups.[26] In the spectrum of the α-Fe_2O_3/

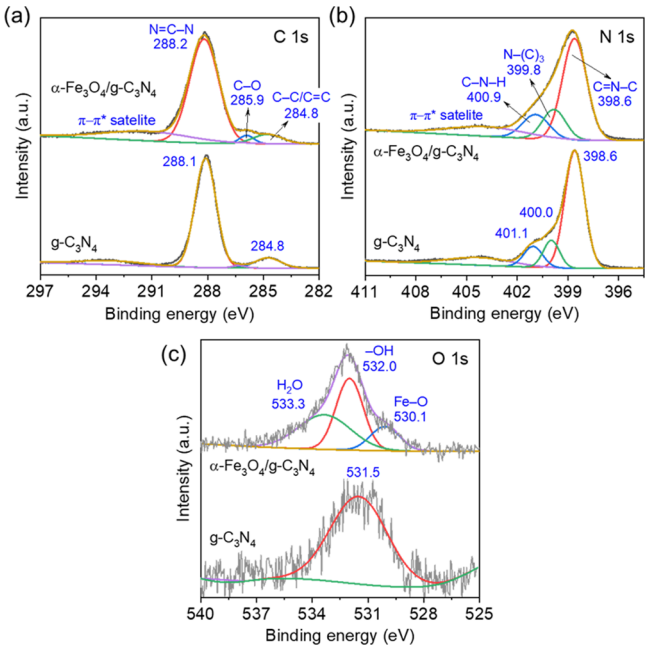

Figure 3. High-resolution XPS spectra of C 1s (a), N 1s (b), and O 1s (c).

g-C_3N_4 composite, three fitted peaks are represented, which are characteristic of lattice oxygen in α-Fe_2O_3 (530.1 eV), the surface hydroxyl groups (532.0 eV),[15,50] and chemisorbed H_2O (533.3 eV).[51] The results of XPS analyses supported the SAED and XRD results to confirm the existence of the α-Fe_2O_3 and graphitic structure of C_3N_4 in the composite sample.

The optical absorption properties of materials were characterized by UV−Vis DRS. As shown in Figure 4a, α-Fe_2O_3 and g-C_3N_4 samples have absorption edges at 676 and 433 nm, respectively. Moreover, the integration of α-Fe_2O_3 with g-C_3N_4 causes a red shift in the absorption edge of α-Fe_2O_3/g-C_3N_4 to 452 nm. This is explained by the synergetic effect between α-Fe_2O_3 and g-C_3N_4, which expands the light

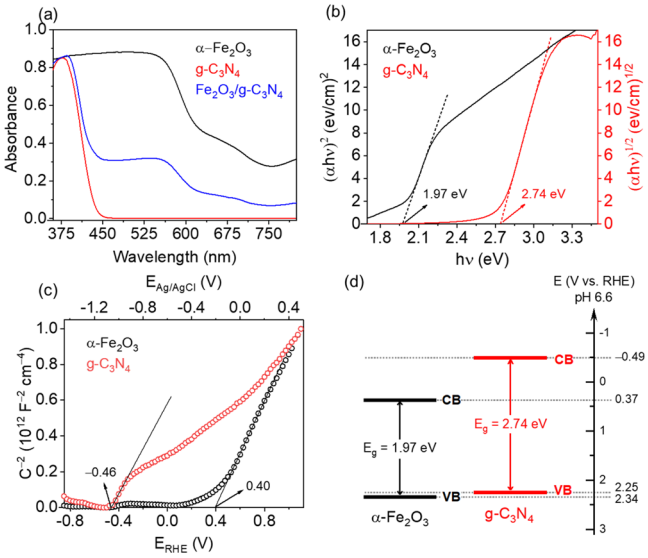

Figure 4. UV−vis DRS spectra (a), Tauc plots (b), Mott−Schottky plots at a frequency of 1 kHz (c), and schematic band structure (d) of α-Fe_2O_3, g-C_3N_4, and α-Fe_2O_3/g-C_3N_4.

https://doi.org/10.1021/acsanm.2c00741
ACS Appl. Nano Mater. XXXX, XXX, XXX−XXX

absorption range of composite material and affirms its good utilization of visible light. For optical band gap determination from UV−Vis DRS spectra and Tauc plots (Figure 4b) were drawn employing Tauc relation

$$\alpha h\nu = A(h\nu - E_g)^{1/n} \quad (1)$$

where α is the absorption coefficient, $h\nu$ is the photon energy, A is the proportionality constant, and E_g is the band gap energy. Depending on whether the nature of transition in the semiconductor is direct or indirect, the value of n is 1/2 or 2, respectively. By extrapolating linear regions to the abscissa, the band gap of α-Fe_2O_3 and g-C_3N_4 is about 1.97 and 2.74 eV, respectively.

To determine the flat-band potential (V_{fb}), which is considered to be too close to the conduction band (CB) edge potential of n-type semiconductors,[10] the Mott−Schottky plot was measured. As illustrated in Figure 4c, the tendency of n-type semiconductors was shown via positive slopes in Mott−Schottky plots of both α-Fe_2O_3 and g-C_3N_4 materials. V_{fb} can be extrapolated from the x-intercept of the linear area of the Mott−Schottky plot via the Mott−Schottky relation. The calculated V_{fb} is 0.37 and −0.49 V versus RHE for α-Fe_2O_3 and g-C_3N_4, respectively (Figure 4c,d). Based on DRS spectra and Mott-Schottky plots, the band structure of the α-Fe_2O_3/g-C_3N_4 composite photocatalyst can be diagramed as shown in Figure 4d. Therein, combining a relatively small band gap (1.97 eV) of α-Fe_2O_3 and a medium band gap (2.74 eV) of g-C_3N_4 will create an advantage in the S-Scheme photocatalyst model established that will be discussed and determined using the following empirical results.

2.2. Photocatalytic Activity Assessment of α-Fe_2O_3/g-C_3N_4. To evaluate the photocatalytic activity and determine the S-scheme model of α-Fe_2O_3/g-C_3N_4, commercial antibiotic pharmaceuticals including cefalexin and amoxicillin were used as contaminant models. The change in typical absorption peaks of cefalexin (260 nm wavelength) and amoxicillin (228 nm wavelength) is recorded and expressed in Figures S3 and S4. In general, all typical absorption peaks of cefalexin and amoxicillin are almost insignificantly shifted during the photocatalytic reaction under visible light irradiation. Figure 5a,b exhibits the photocatalytic degradation of cefalexin over pure g-C_3N_4 and α-Fe_2O_3/g-C_3N_4 with different percentages of α-Fe_2O_3. The photolysis of cefalexin and amoxicillin was also tested in the absence of catalysts, and the results indicated that these antibiotics are quite stable and insignificantly degraded without the presence of photocatalysts under visible light illumination. There seems to be a general rule in the photocatalysis of cefalexin and amoxicillin. In detail, the photocatalytic activity of both pure α-Fe_2O_3 and g-C_3N_4 is not good for the degradation of both cefalexin and amoxicillin. This could be explained due to the rapid recombination of photoinduced electron−hole pairs in narrow-band gap materials such as α-Fe_2O_3 (1.97 eV).[25] Although the band gap of g-C_3N_4 (2.74 eV) is larger than that of α-Fe_2O_3, valence band (VB) edge potential position (Figure 4d) of g-C_3N_4 is still disadvantageous for the degradation of cephalexin, leading to a weak activity (23.9%). When α-Fe_2O_3 is modified with g-C_3N_4, the photocatalytic activity of g-C_3N_4 is significantly improved, and the best activity is achieved with 5% α-Fe_2O_3. The enhancement in photocatalytic performance is due to the synergetic effect between α-Fe_2O_3 and g-C_3N_4, which helps photoinduced carriers to separate effectively and broadens the light

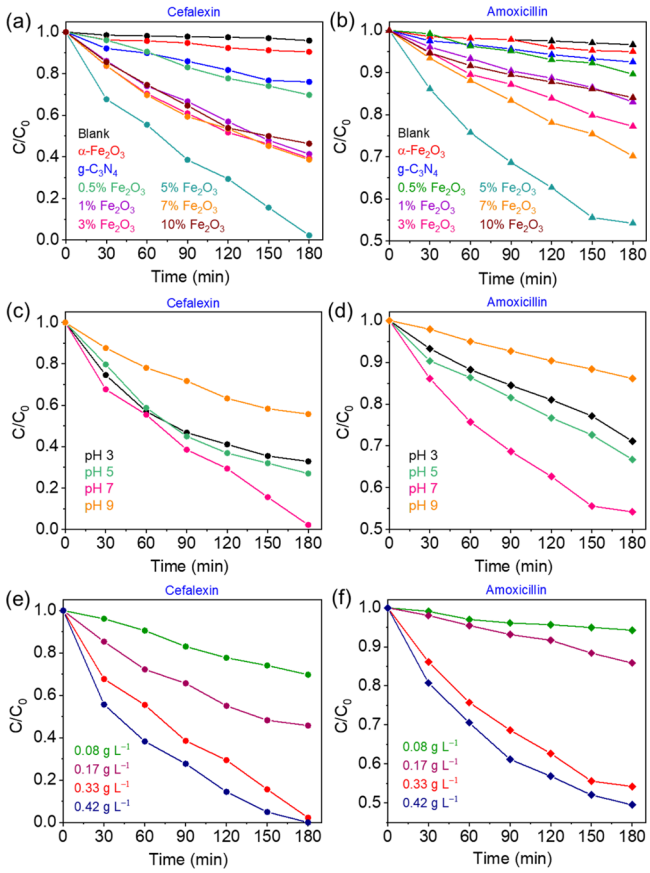

Figure 5. Photocatalytic degradation of cefalexin (a) and amoxicillin (b) over α-Fe_2O_3, g-C_3N_4, and α-Fe_2O_3/g-C_3N_4 composites with various α-Fe_2O_3 percentages and initial pH dependence on the photocatalytic degradation of cefalexin (c) and amoxicillin (d) over α-Fe_2O_3/g-C_3N_4 ([pharmaceuticals]$_0$ = 20 mg L^{-1} and [photocatalyst]$_0$ = 0.33 g L^{-1}]); photocatalytic removal of cefalexin (e) and amoxicillin (f) with various amounts of α-Fe_2O_3/g-C_3N_4 ([pharmaceuticals]$_0$ = 20 mg L^{-1}).

absorption range of the composite material. However, when α-Fe_2O_3 content in the composites exceeds 5 wt %, the photocatalytic performance tends to decrease. This could be explained by the light-shield effect caused by α-Fe_2O_3, which inhibits the light harvesting of matrix material g-C_3N_4. The investigation on photocatalytic degradation of cefalexin and amoxicillin was also carried out with the same approach, indicating a superior performance of the α-Fe_2O_3/g-C_3N_4 composites in the cefalexin degradation that is more efficient than that of the amoxicillin case. Furthermore, the pseudo-first-order kinetics following the Langmuir−Hinshelwood (L−H) model of the degradation processes of cefalexin and amoxicillin are also calculated and presented in Figure S5. It was found that the photocatalytic reaction rate constant (k) values for the photocatalytic degradation of cefalexin (a) and amoxicillin achieved the maximum value 112.80×10^{-4} min^{-1} and 40.20×10^{-4} min^{-1} over 5% α-Fe_2O_3/g-C_3N_4, respectively (Table S1). From these investigations, we choose the 5% α-Fe_2O_3/g-C_3N_4 composite to survey for the subsequent experiments. For instance, the effect of the pH value of the antibiotic solution on the photocatalytic activity of the 5% α-Fe_2O_3/g-C_3N_4 composite is tested and displayed in Figure 5c. The photocatalytic activity of α-Fe_2O_3/g-C_3N_4 for cefalexin degradation at various pH values indicated that the best

https://doi.org/10.1021/acsanm.2c00741
ACS Appl. Nano Mater. XXXX, XXX, XXX−XXX

Table 1. Comparison of Some Photocatalytic Systems Degrading Cefalexin and Amoxicillin

photocatalytic system	antibiotic	antibiotic conc. (mg L^{-1})	catalyst dosage (g L^{-1})	irradiation time (min)	photocatalytic efficiency (%)	refs
g-C_3N_4@ZnO/sunlight	cefalexin	10	0.3	60	98.9	54
$CuWO_4/Bi_2S_3$/Vis	cefalexin	10	0.8	150	76	55
g-C_3N_4/ZnFe/Vis	cefalexin	10	0.05	300	91	56
N−$TiO_2/ZnFe_2O_4$/zeolite/UV−vis	cefalexin	100	2	120	74	57
Bi_2WO_6/CNT/TiO_2/sunlight	cefalexin	20	0.75	70	89.7	58
α-Fe_2O_3/g-C_3N_4/vis	**cefalexin**	**20**	**0.33**	**120**	**71**	**this work**
				180	**98**	
mesoporous g-C_3N_4/vis	amoxicillin	2	1	60	96	59
CQDs/$K_2Ti_6O_{13}$/vis	amoxicillin	1	2	90	73.6	60
WO_3/vis	amoxicillin	1.2	0.104	180	99.99	61
α-Fe_2O_3/g-C_3N_4/vis	**amoxicillin**	**20**	**0.33**	**180**	**46**	**this work**

degradation efficiency (97.8%) of cefalexin is obtained at pH 7, which is 1.5, 1.3, and 2.2 times higher than that at pH 3 (67.1%), pH 5 (72.9%), and pH 9 (44.2%). For amoxicillin, the optimal pH value for photocatalytic degradation over α-Fe_2O_3/g-C_3N_4 is also confirmed to be neutral (Figure 5d). These results verify that α-Fe_2O_3/g-C_3N_4 works well in the wide environmental pH range. Therein, the neutral solution is the best medium for the photocatalysis of α-Fe_2O_3/g-C_3N_4 that also showed a reaction rate of 112.80×10^{-4} min^{-1} and 40.20×10^{-4} min^{-1} for cefalexin and amoxicillin degradation, respectively (Table S2). In addition, the influence of catalyst amount on the photocatalytic removal process is also studied in this study. As presented in Figure 5e,f, the increase in α-Fe_2O_3/g-C_3N_4 amount is accompanied by the enhancement in photocatalytic degradation of antibiotics. This could be primarily explained by the increase in target molecules (O_2, H_2O, and antibiotics) adsorbed on the photocatalyst surface. Meanwhile, under visible light conditions, the generation of active species should also be boosted. These results indicate that the amount of catalysts also plays a critical role in photocatalytic activity. In addition, the constant rate k of the degradation processes of cefalexin and amoxicillin is also calculated and presented in Figure S6 and Table S3.

In addition to photocatalytic performance, photocatalyst stability is also of vital importance for potential practical application. The photocatalytic recycling stability after five cycles of α-Fe_2O_3/g-C_3N_4 for the degradation of cefalexin and amoxicillin solution, respectively, is shown in Figure S7a,b. The α-Fe_2O_3/g-C_3N_4 exhibits a relatively stable photocatalytic removal of the antibiotics, which declines only slightly after five photocatalytic cycles. Additionally, the FITR spectrum of the material after the reusability test (Figure S7c) is presented in the Supporting Information. Additionally, a comparison of some photocatalytic systems degrading cefalexin and amoxicillin is shown in Table 1. In addition, the Fe-ion concentration in samples before and after the photocatalytic reaction has been determined by inductively coupled plasma-atomic emission spectrometry (ICP-EOS). Therein, the Fe-ion concentration in samples before and after the photocatalytic reaction is less changed with 3.28 and 3.49%, respectively. Clearly, the α-Fe_2O_3/g-C_3N_4 composite is a potential material for the efficient degradation of the high concentration of antibiotics with a small amount of the catalysts.

2.3. Empirical Evidence for an S-Scheme Photocatalyst Model of α-Fe_2O_3/g-C_3N_4. To further determine the active species that mainly function in the photocatalytic degradation of cefalexin and amoxicillin, the active-species trapping tests were carried out. Figure 6a illustrates the decreases in antibiotic removal after the addition of $K_2Cr_2O_7$,

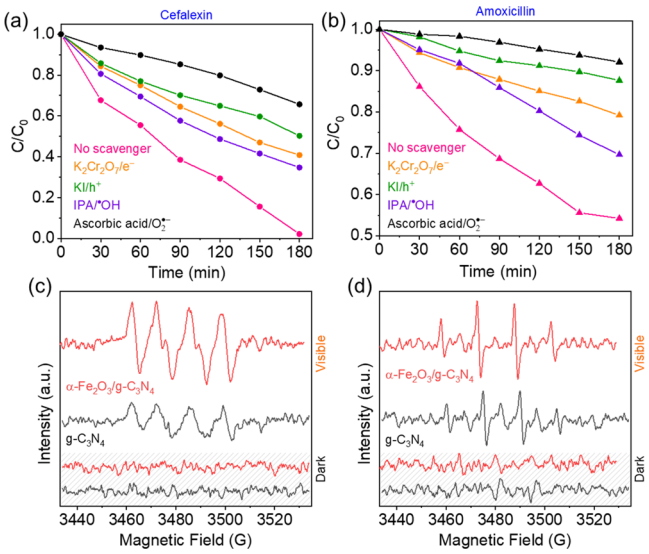

Figure 6. Influence of scavengers on photocatalytic degradation of cefalexin (a) and amoxicillin (b) over α-Fe_2O_3/g-C_3N_4 ([photocatalyst]$_0$ = 0.33 g L^{-1} and [pharmaceuticals]$_0$ = 20 mg L^{-1}) and DMPO−$^{\bullet}O_2^-$ (c) and DMPO−$^{\bullet}OH$ (d) EPR spectra over g-C_3N_4 and α-Fe_2O_3/g-C_3N_4.

KI, IPA, and ascorbic acid as electron (e^-), hole (h^+), $^{\bullet}OH$, and $^{\bullet}O_2^-$ quenchers, respectively, which reveal that the visible light-induced photocatalytic activity of the α-Fe_2O_3/g-C_3N_4 composite is governed by e^-, h^+, $^{\bullet}OH$, and $^{\bullet}O_2^-$. The considerable decreases in the removal of the antibiotics (Figure 6a,b) and the rate constant k (Figure S8) triggered by KI also indicate that h^+ radicals primarily dominate photocatalytic reactions. It is easy to see that ascorbic acid and KI significantly decreased the photocatalytic ability of the α-Fe_2O_3/g-C_3N_4 composite for both cefalexin and amoxicillin degradation. The rate constant of the photocatalytic reaction was also calculated (Table S4) and demonstrated that the existence of all scavengers inhibited the breakdown of antibiotic compounds. From the active-radical trapping test results, we can conclude that the $^{\bullet}O_2^-$ and h^+ are primary parameters for the photocatalytic degradation of cefalexin and amoxicillin. Besides, Figure 6c,d shows the DMPO spin-trapping EPR spectra of g-C_3N_4 and α-Fe_2O_3/g-C_3N_4 with almost no signal in the dark. Under visible light, the signals of

https://doi.org/10.1021/acsanm.2c00741
ACS Appl. Nano Mater. XXXX, XXX, XXX−XXX

$^{\bullet}O_2^-$ and $^{\bullet}OH$ are clearer, proving the existence of these active species in the photocatalytic systems containing g-C_3N_4 and α-Fe_2O_3/g-C_3N_4. Notably, the $^{\bullet}O_2^-$ and $^{\bullet}OH$ signals are sharper for the composite spectrum than for the g-C_3N_4 spectrum. This finding reinforces the proposed S-scheme charge transfer mechanism in α-Fe_2O_3/g-C_3N_4, which is beneficial for the photocatalytic efficiency of the composites compared with the raw constituent materials.

When absorbing light energy greater than or equal to the band gap of each component photocatalyst, photogenerated charge carriers are produced in their respective CB and VB. However, the unfavorable CB edge energy for the reduction of molecular O_2 to $^{\bullet}O_2^-$ of α-Fe_2O_3 and the VB edge position are more negative than the redox potential of $H_2O/^{\bullet}OH$ of g-C_3N_4, making them poor photocatalysts.[24] Therefore, a typical type-II charge transfer process that causes the transfer of photoinduced holes (h^+) from the VB of α-Fe_2O_3 to the VB of g-C_3N_4 and electrons (e^-) from the CB of g-C_3N_4 down to that of α-Fe_2O_3 could even hinder the photocatalytic activity of the composite compared to the pristine materials. From the results in Figure 4d, an arrangement of band structures of α-Fe_2O_3 and g-C_3N_4 is an advantage for suggesting an S-scheme mechanism for the degradation of antibiotics over the α-Fe_2O_3/g-C_3N_4 composite, as regards the above experimental results (Figure 7). As g-C_3N_4 with lower work functions and α-Fe_2O_3 with higher work functions come in contact,[24,52] electrons in g-C_3N_4 will flow to α-Fe_2O_3 until their new Fermi level is aligned at equilibrium. Consequently, the formation of positively charged g-C_3N_4 and negatively charged α-Fe_2O_3 at the α-Fe_2O_3/g-C_3N_4 interface took place, which formed an internal electric field. Meanwhile, the band edge bending occurred for two semiconductors. Therein, g-C_3N_4 will bend the band edge uphill while α-Fe_2O_3 will curve its band edge downhill. This S-scheme charge transfer process orients efficiently the movement of electron−hole pairs, which facilitates the recombination of useless photogenerated e− in the α-Fe_2O_3 CB and h^+ in the g-C_3N_4 VB via d-p conjugation and retains useful charge carriers within each component material. In addition, α-Fe_2O_3 also contributes to the photocatalytic reaction throughout the reduction of Fe^{3+} to Fe^{2+} to form the $^{\bullet}OH$ active radical (eq 7) that has been reported by Meng et al.[53] Thus, the photocatalytic efficiency is significantly improved. The photoinduced electrons in the g-C_3N_4 CB and holes in the α-Fe_2O_3 VB will migrate to their surface to participate in the O_2 reduction and be consumed in H_2O oxidation, respectively, to produce $^{\bullet}O_2^-$ and $^{\bullet}OH$ active radicals that involved in the antibiotic degradation (eqs 2−8). The α-Fe_2O_3/g-C_3N_4 heterojunction has improved the carrier separation efficiency, thereby reducing the possibility of electron−hole recombination, which is expressed in Figure S10. Therein, the photocurrent density of α-Fe_2O_3/g-C_3N_4 is five times higher than that of the individual α-Fe_2O_3 under visible light illumination. Figure 6 demonstrates the formation of primary reactive radicals of $^{\bullet}O_2^-$ and $^{\bullet}OH$, which makes this S-scheme model superior in charge transport during photocatalysis. Moreover, the degradation of amoxicillin and cefalexin over Fe_2O_3/g-C_3N_4 is nearly complete, which was demonstrated by HPLC-MS chromatograms of amoxicillin and cefalexin before and after the photocatalytic reaction (Figure S11). After the photocatalytic reaction, the primary compounds of amoxicillin and cefalexin almost disappeared and formed products with smaller molecular formulas. This proves that the α-Fe_2O_3/g-C_3N_4 nanocomposite has very high efficiency in decomposing antibiotics.

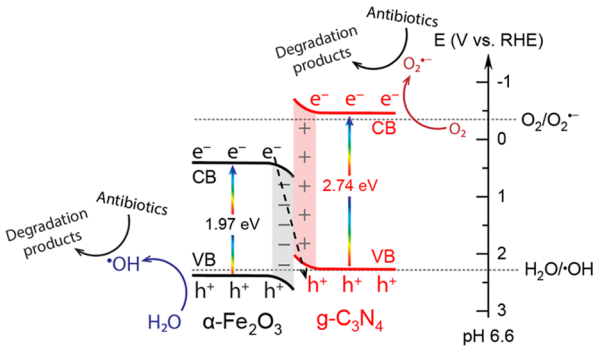

Figure 7. Proposed mechanism for photocatalytic degradation of antibiotics over S-scheme α-Fe_2O_3/g-C_3N_4.

$$\alpha\text{-Fe}_2\text{O}_3/\text{g-C}_3\text{N}_4 + h\nu \rightarrow \alpha\text{-Fe}_2\text{O}_3/\text{g-C}_3\text{N}_4(e^- + h^+) \quad (2)$$

$$e^- + \text{antibiotics} \rightarrow \text{antibiotics}^-(\text{direct oxidation of antibiotics}) \quad (3)$$

$$e^- + O_2 \rightarrow {}^{\bullet}O_2^- \quad (4)$$

$$^{\bullet}O_2^- + e^- + 2H^+ \rightarrow H_2O_2 \quad (5)$$

$$Fe^{3+} + H_2O \rightarrow Fe^{2+} + HO^{\bullet} + H \quad (6)$$

$$H_2O_2 + e^- \rightarrow HO^{\bullet} + HO^- \quad (7)$$

$$h^+ + \text{antibiotics} \rightarrow \text{antibiotics}^+(\text{direct oxidation of antibiotics}) \quad (8)$$

3. CONCLUSIONS

In conclusion, α-Fe_2O_3/g-C_3N_4 nanocomposites were successfully prepared by two-step simple processes, and this material is used to degrade commercial cefalexin and amoxicillin for the first time. Modifying 5% wt α-Fe_2O_3 significantly improves the photocatalytic activity of g-C_3N_4 with a fivefold and ninefold enhancement in performance for commercial cefalexin and amoxicillin degradation compared to that by only using g-C_3N_4. In addition, the $^{\bullet}O_2^-$ and $^{\bullet}OH$ radicals are the primary active species in the photocatalytic degradation of commercial cefalexin and amoxicillin. This is an empirical result to confirm the performance an S-scheme α-Fe_2O_3/g-C_3N_4 heterojunction. Moreover, the high stability of the α-Fe_2O_3/g-C_3N_4 photocatalyst is also an advantage that can be applied under practical conditions.

4. EXPERIMENTAL PROCEDURES

4.1. Chemicals and Materials. All chemicals, iron(III) nitrate nonahydrate ($Fe(NO_3)_3{\cdot}9H_2O$), gelatin ($C_{102}H_{151}O_{39}N_{31}$), melamine ($C_3H_6N_6$), ethanol ($C_2H_6O$), potassium dichromate ($K_2Cr_2O_7$), potassium iodide (KI), isopropyl alcohol (IPA; C_3H_8O), ascorbic acid ($C_6H_8O_6$), and deionized water (DI), were of high purity and used without further purification. The commercial cefalexin and amoxicillin originated from the DHG Pharmaceutical Joint Stock Company (Vietnam).

4.2. Preparation of g-C_3N_4. Melamine was employed as a precursor to prepare g-C_3N_4 through a thermal polycondensation approach. In detail, 2 g of melamine was added to a ceramic crucible

https://doi.org/10.1021/acsanm.2c00741
ACS Appl. Nano Mater. XXXX, XXX, XXX−XXX

and calcined at 500 °C for 2 h in a furnace (JS Research, JSMF-30T) under the inserted argon gas at a heating rate of 2 °C min^{-1}.

4.3. Synthesis of α-Fe_2O_3. α-Fe_2O_3 was synthesized by a sol−gel method, in which $Fe(NO_3)_3{\cdot}9H_2O$ and gelatin were utilized as a precursor and a polymerization agent, respectively. First, 4 g of $Fe(NO_3)_3{\cdot}9H_2O$ was dissolved in 100 mL of DI for 30 min to form solution A. Solution B consisted of 1.5 g of gelatin in 100 mL of DI and stirred for 30 min. Second, solution B was slowly poured into solution A and continuously stirred for 1 h for gel formation. Third, the gel mixture was dried at 60 °C for 6 h. Finally, the obtained powder was calcined at 600 °C for 1 h in the air.

4.4. Synthesis of α-Fe_2O_3/g-C_3N_4 Nanocomposites. α-Fe_2O_3/g-C_3N_4 photocatalysts were synthesized, referencing the previous report of Houli et al.[35] Briefly, g-C_3N_4 powder was uniformly dispersed in ethanol by sonication. α-Fe_2O_3 and a Nafion solution were then added to the above suspension and further sonicated for 1 h. The resulting mixtures of α-Fe_2O_3/g-C_3N_4 were centrifuged, washed, and dried at 60 °C for 12 h. The composite samples with different theoretical weight percentages of α-Fe_2O_3 were denoted as x % α-Fe_2O_3 (x = 0.5, 1, 3, 7, and 10).

4.5. Sample Characterizations. X-ray powder diffraction (XRD) patterns of the as-prepared materials were recorded using an X-ray powder diffractometer (Bruker D8 Advance with Cu-Kα radiation). The characteristic bond vibrations of photocatalysts were determined using a JASCO-4700 Fourier-transform infrared (FTIR) spectrometer. The oxidation states of samples were analyzed using an X-ray photoelectron spectrometer (XPS) (K-Alpha, Thermo Fisher Scientific). The ultraviolet−visible diffuse reflectance spectra (UV−vis DRS) characterization of powder samples was conducted employing a JASCO V−550 spectrophotometer. The surface morphology of materials was observed through scanning electron microscopy (SEM, JEOL JSM-IT500) and high-resolution transmission electron microscopy (HRTEM, JEOL JEM-2100). Electron paramagnetic resonance (EPR) measurement was carried out on a Bruker EMXPlus EPR spectrometer with X-band capabilities. The electrochemical experiments were performed on a galvanostat (BioLogic SP-200), with a three-electrode system [the as-prepared sample working electrode with an area of 0.5 × 1 cm^2, a Pt wire counter electrode, and an Ag/AgCl (3.0 M KCl) reference electrode]. 0.5 M Na_2SO_4 solution was used as the electrolyte. The Fe-ion concentration in water before and after photocatalytic degradation was determined by inductively coupled plasma-atomic emission spectrometry (ICP-EOS).

4.6. Photocatalytic Degradation Experiment. Photocatalytic activities of the as-prepared samples were assessed by degrading the commercial antibiotic pharmaceuticals cefalexin and amoxicillin under visible light illumination at room temperature. In a typical experiment, 0.02 g of the catalyst was dispersed into 60 mL of pharmaceutical solution (20 mg L^{-1}). Before shining the light, the adsorption process was conducted for 120 min in the dark to obtain adsorption−desorption equilibrium (Figure S12). After that, the suspension was irradiated under a solar simulator (OSRAM ULTRA VITALUX 300W with a UV cutoff filter, λ > 420 nm) as a visible light source. The suspension was sampled at regular intervals of 30 min and centrifuged to acquire a clear liquid. The remaining concentrations of pharmaceuticals were detected using a UV−vis spectrophotometer (Hitachi U-2910). For the assessment of pH-dependent photocatalytic activity, initial pH values of pharmaceutical solution were adjusted with the solution of H_2SO_4 and NaOH.

Active-species trapping tests were performed similar to the photocatalytic degradation experiment, with the addition of $K_2Cr_2O_7$, KI, IPA, and ascorbic acid as the scavengers. For appraising the stability and reusability of material, the photocatalyst was separated from the photoreactor after each cycle and photocatalytic degradation processes were repeated under the same conditions. The mineral level and the possible degradation of antibiotics were identified by liquid chromatography−mass spectrometry (HPLC-MS) over an Agilent 6200 Series TOF system and a 6500 Series Q-TOF LC/MS system.

■ ASSOCIATED CONTENT

Supporting Information

The Supporting Information is available free of charge at https://pubs.acs.org/doi/10.1021/acsanm.2c00741.

SEM images of α-Fe_2O_3, g-C_3N_4, and α-Fe_2O_3/g-C_3N_4; XPS survey spectra of g-C_3N_4 and α-Fe_2O_3/g-C_3N_4; UV−vis absorption spectra for the typical degradation process of cefalexin and amoxicillin under visible light; pseudo-first order kinetic fitting curves and calculation data tables for the photocatalysis; photocatalytic degradation toward cefalexin and amoxicillin after five cycles; FTIR spectra of α-Fe_2O_3/g-C_3N_4 before and after recycling test; photocurrent response of materials; adsorption ability of cefalexin and amoxicillin over the surface of materials; and HPLC-MS chromatograms of amoxicillin and cefalexin in the before case and after photocatalytic reaction (PDF)

■ AUTHOR INFORMATION

Corresponding Author

Thi Minh Cao − *HUTECH University, Ho Chi Minh City 700000, Vietnam;* orcid.org/0000-0001-9323-2326; Email: cmthi@hutech.edu.vn

Authors

Viet Van Pham − *University of Science, VNU-HCM, Ho Chi Minh City 700000, Vietnam; Vietnam National University Ho Chi Minh City, Ho Chi Minh City 700000, Vietnam;* orcid.org/0000-0002-8697-7095

Thao Kim Truong − *University of Science, VNU-HCM, Ho Chi Minh City 700000, Vietnam; Vietnam National University Ho Chi Minh City, Ho Chi Minh City 700000, Vietnam;* orcid.org/0000-0003-0145-2415

Le Viet Hai − *University of Science, VNU-HCM, Ho Chi Minh City 700000, Vietnam; Vietnam National University Ho Chi Minh City, Ho Chi Minh City 700000, Vietnam*

Ha Phan Phuong La − *University of Science, VNU-HCM, Ho Chi Minh City 700000, Vietnam; Vietnam National University Ho Chi Minh City, Ho Chi Minh City 700000, Vietnam*

Hoang Thai Nguyen − *University of Science, VNU-HCM, Ho Chi Minh City 700000, Vietnam; Vietnam National University Ho Chi Minh City, Ho Chi Minh City 700000, Vietnam*

Vinh Quang Lam − *Vietnam National University Ho Chi Minh City, Ho Chi Minh City 700000, Vietnam*

Hien Duy Tong − *Faculty of Engineering, Vietnamese-German University (VGU), Thu Dau Mot City, Binh Duong Province 75000, Vietnam*

Thang Quoc Nguyen − *Institute of Atomic and Molecular Science, Academia Sinica, Taipei 16017, Taiwan*

Amr Sabbah − *Institute of Atomic and Molecular Science, Academia Sinica, Taipei 16017, Taiwan*

Kuei-Hsien Chen − *Institute of Atomic and Molecular Science, Academia Sinica, Taipei 16017, Taiwan;* orcid.org/0000-0002-9397-2516

Sheng-Jie You − *Department of Environmental Engineering, Chung Yuan Christian University, Taoyuan 32023, Taiwan*

Complete contact information is available at: https://pubs.acs.org/10.1021/acsanm.2c00741

Notes

The authors declare no competing financial interest.

■ ACKNOWLEDGMENTS

The authors would like to thank Vietnam National University-Ho Chi Minh City (VNU-HCM) for the financial support. We sincerely thank Nguyen Thi Thuy Vy for the initial experimental setup.

■ REFERENCES

(1) Wang, B.; Li, H.; Liu, T.; Guo, J. Enhanced removal of cephalexin and sulfadiazine in nitrifying membrane-aerated biofilm reactors. *Chemosphere* **2021**, *263*, 128224.

(2) Bian, X.; Xia, Y.; Zhan, T.; Wang, L.; Zhou, W.; Dai, Q.; Chen, J. Electrochemical removal of amoxicillin using a Cu doped PbO2 electrode: Electrode characterization, operational parameters optimization and degradation mechanism. *Chemosphere* **2019**, *233*, 762−770.

(3) Blaser, M. J. Antibiotic use and its consequences for the normal microbiome. *Science* **2016**, *352*, 544−545.

(4) Yang, Y.; Song, W.; Lin, H.; Wang, W.; Du, L.; Xing, W. Antibiotics and antibiotic resistance genes in global lakes: A review and meta-analysis. *Environ. Int.* **2018**, *116*, 60−73.

(5) Brown, E. D.; Wright, G. D. Antibacterial drug discovery in the resistance era. *Nature* **2016**, *529*, 336−343.

(6) Abellán, M. N.; Giménez, J.; Esplugas, S. Photocatalytic degradation of antibiotics: The case of sulfamethoxazole and trimethoprim. *Catal. Today* **2009**, *144*, 131−136.

(7) Moradi, M.; Hasanvandian, F.; Isari, A. A.; Hayati, F.; Kakavandi, B.; Setayesh, S. R. CuO and ZnO co-anchored on g-C_3N_4 nanosheets as an affordable double Z-scheme nanocomposite for photocatalytic decontamination of amoxicillin. *Appl. Catal., B* **2021**, *285*, 119838.

(8) Yang, C.; You, X.; Cheng, J.; Zheng, H.; Chen, Y. A novel visible-light-driven In-based MOF/graphene oxide composite photocatalyst with enhanced photocatalytic activity toward the degradation of amoxicillin. *Appl. Catal., B* **2017**, *200*, 673−680.

(9) Sun, X.; He, W.; Yang, T.; Ji, H.; Liu, W.; Lei, J.; Liu, Y.; Cai, Z. Ternary TiO_2/WO_3/CQDs nanocomposites for enhanced photocatalytic mineralization of aqueous cephalexin: Degradation mechanism and toxicity evaluation. *Chem. Eng. J.* **2021**, *412*, 128679.

(10) Truong, T. K.; Nguyen, T. Q.; Phuong La, H. P.; Le, H. V.; Van Man, T.; Cao, T. M.; Van Pham, V. Insight into the degradation of p-nitrophenol by visible-light-induced activation of peroxymonosulfate over Ag/ZnO heterojunction. *Chemosphere* **2021**, *268*, 129291.

(11) Truong, T. K.; Van Doan, T.; Tran, H. H.; Van Le, H.; Lam, V. Q.; Tran, H. N.; Cao, T. M.; Van Pham, V. Effect of Cr Doping on Visible-Light-Driven Photocatalytic Activity of ZnO Nanoparticles. *J. Electron. Mater.* **2019**, *48*, 7378−7388.

(12) Niu, P.; Li, L. Photocatalytic overall water splitting of carbon nitride by band-structure modulation. *Matter* **2021**, *4*, 1765−1767.

(13) Su, T.; Shao, Q.; Qin, Z.; Guo, Z.; Wu, Z. Role of Interfaces in Two-Dimensional Photocatalyst for Water Splitting. *ACS Catal.* **2018**, *8*, 2253−2276.

(14) Thang, N. Q.; Sabbah, A.; Chen, L.-C.; Chen, K.-H.; Hai, L. V.; Thi, C. M.; Viet, P. V. Localized surface plasmonic resonance role of silver nanoparticles in the enhancement of long-chain hydrocarbons of the CO_2 reduction over Ag-gC_3N_4/ZnO nanorods photocatalysts. *Chem. Eng. Sci.* **2021**, *229*, 116049.

(15) Thang, N. Q.; Sabbah, A.; Chen, L.-C.; Chen, K.-H.; Thi, C. M.; Van Viet, P. High-efficient photocatalytic degradation of commercial drugs for pharmaceutical wastewater treatment prospects: A case study of Ag/g-C_3N_4/ZnO nanocomposite materials. *Chemosphere* **2021**, *282*, 130971.

(16) Van Pham, V.; Mai, D.-Q.; Bui, D.-P.; Van Man, T.; Zhu, B.; Zhang, L.; Sangkaworn, J.; Tantirungrotechai, J.; Reutrakul, V.; Cao, T. M. Emerging 2D/0D g-C_3N_4/SnO_2 S-scheme photocatalyst: New generation architectural structure of heterojunctions toward visible-light-driven NO degradation. *Environ. Pollut.* **2021**, *286*, 117510.

(17) Wang, W.; Fang, J.; Shao, S.; Lai, M.; Lu, C. Compact and uniform TiO2@g-C_3N_4 core-shell quantum heterojunction for photocatalytic degradation of tetracycline antibiotics. *Appl. Catal., B* **2017**, *217*, 57−64.

(18) Guo, H.; Chen, M.; Zhong, Q.; Wang, Y.; Ma, W.; Ding, J. Synthesis of Z-scheme α-Fe_2O_3/g-C_3N_4 composite with enhanced visible-light photocatalytic reduction of CO_2 to CH_3OH. *J. CO2 Util.* **2019**, *33*, 233−241.

(19) Mamba, G.; Mishra, A. K. Graphitic carbon nitride (g-C_3N_4) nanocomposites: A new and exciting generation of visible light driven photocatalysts for environmental pollution remediation. *Appl. Catal., B* **2016**, *198*, 347−377.

(20) Liu, W.; Sun, M.; Ding, Z.; Gao, B.; Ding, W. Ti_3C_2 MXene embellished g-C_3N_4 nanosheets for improving photocatalytic redox capacity. *J. Alloys Compd.* **2021**, *877*, 160223.

(21) Van Viet, P.; Van Chuyen, D.; Hien, N. Q.; Duy, N. N.; Thi, C. M. Visible-light-induced photo-Fenton degradation of rhodamine B over Fe_2O_3-diatomite materials. *J. Sci.: Adv. Mater. Devices* **2020**, *5*, 308−315.

(22) Cui, H.; Liu, Y.; Ren, W. Structure switch between α-Fe_2O_3, γ-Fe_2O_3 and Fe_3O_4 during the large scale and low temperature sol−gel synthesis of nearly monodispersed iron oxide nanoparticles. *Adv. Powder Technol.* **2013**, *24*, 93−97.

(23) Malato-Rodríguez, S. Solar Detoxification and Disinfection. *Encyclopedia of Energy*; Elsevier Academic Press, 2004; pp 587−596.

(24) Xu, Q.; Zhu, B.; Jiang, C.; Cheng, B.; Yu, J. Constructing 2D/2D Fe_2O_3/g-C_3N_4 Direct Z-Scheme Photocatalysts with Enhanced H_2 Generation Performance. *Sol. RRL* **2018**, *2*, 1800006.

(25) She, X.; Wu, J.; Xu, H.; Zhong, J.; Wang, Y.; Song, Y.; Nie, K.; Liu, Y.; Yang, Y.; Rodrigues, M.-T. F.; Vajtai, R.; Lou, J.; Du, D.; Li, H.; Ajayan, P. M. High Efficiency Photocatalytic Water Splitting Using 2D α-Fe_2O_3/g-C_3N_4 Z-Scheme Catalysts. *Adv. Energy Mater.* **2017**, *7*, 1700025.

(26) Li, Y.; Zhu, S.; Liang, Y.; Li, Z.; Wu, S.; Chang, C.; Luo, S.; Cui, Z. Synthesis of α-Fe_2O_3/g-C_3N_4 photocatalyst for high-efficiency water splitting under full light. *Mater. Des.* **2020**, *196*, 109191.

(27) Arzaee, N. A.; Mohamad Noh, M. F.; Mohd Ita, N. S. H.; Mohamed, N. A.; Mohd Nasir, S. N. F.; Nawas Mumthas, I. N.; Ismail, A. F.; Mat Teridi, M. A. Nanostructure-assisted charge transfer in alpha-Fe_2O_3/g-C_3N_4 heterojunctions for efficient and highly stable photoelectrochemical water splitting. *Dalton Trans.* **2020**, *49*, 11317−11328.

(28) Jiang, Z.; Wan, W.; Li, H.; Yuan, S.; Zhao, H.; Wong, P. K. A Hierarchical Z-Scheme alpha-Fe_2O_3/g-C_3N_4 Hybrid for Enhanced Photocatalytic CO_2 Reduction. *Adv. Mater.* **2018**, *30*, 1706108.

(29) Duan, B.; Mei, L. A Z-scheme Fe_2O_3/g-C_3N_4 heterojunction for carbon dioxide to hydrocarbon fuel under visible illuminance. *J. Colloid Interface Sci.* **2020**, *575*, 265−273.

(30) Shen, Y.; Han, Q.; Hu, J.; Gao, W.; Wang, L.; Yang, L.; Gao, C.; Shen, Q.; Wu, C.; Wang, X.; Zhou, X.; Zhou, Y.; Zou, Z. Artificial Trees for Artificial Photosynthesis: Construction of Dendrite-Structured α-Fe_2O_3/g-C_3N_4 Z-Scheme System for Efficient CO_2 Reduction into Solar Fuels. *ACS Appl. Energy Mater.* **2020**, *3*, 6561−6572.

(31) Xiao, D.; Dai, K.; Qu, Y.; Yin, Y.; Chen, H. Hydrothermal synthesis of α-Fe_2O_3/g-C3N4 composite and its efficient photocatalytic reduction of Cr(VI) under visible light. *Appl. Surf. Sci.* **2015**, *358*, 181−187.

(32) Sun, S.; Ji, C.; Wu, L.; Chi, S.; Qu, R.; Li, Y.; Lu, Y.; Sun, C.; Xue, Z. Facile one-pot construction of α-Fe_2O_3/g-C_3N_4 heterojunction for arsenic removal by synchronous visible light catalysis oxidation and adsorption. *Mater. Chem. Phys.* **2017**, *194*, 1−8.

(33) Christoforidis, K. C.; Montini, T.; Bontempi, E.; Zafeiratos, S.; Jaén, J. J. D.; Fornasiero, P. Synthesis and photocatalytic application of visible-light active β -Fe_2O_3/g-C_3N_4 hybrid nanocomposites. *Appl. Catal., B* **2016**, *187*, 171−180.

(34) Singh, J.; Basu, S. Synthesis of mesoporous magnetic Fe_2O_3/g-C_3N_4 monoliths for Rhodamine B removal. *Microporous Mesoporous Mater.* **2020**, *303*, 110299.

https://doi.org/10.1021/acsanm.2c00741
ACS Appl. Nano Mater. XXXX, XXX, XXX−XXX

(35) Zhang, H.; Zhu, C.; Cao, J.; Tang, Q.; Li, M.; Kang, P.; Shi, C.; Ma, M. Ultrasonic-Assisted Synthesis of 2D α-Fe_2O_3@g-C_3N_4 Composite with Excellent Visible Light Photocatalytic Activity. *Catalysts* **2018**, *8*, 457.
(36) Zuo, S.; Xia, D.; Guan, Z.; Yang, F.; Zhang, B.; Xu, H.; Huang, M.; Guo, X.; Li, D. The polarized electric field on Fe_2O_3/g-C_3N_4 for efficient peroxymonosulfate activation: A synergy of $^1O_2$, electron transfer and pollutant oxidation. *Sep. Purif. Technol.* **2021**, *269*, 118717.
(37) Wang, T.; Huang, M.; Liu, X.; Zhang, Z.; Liu, Y.; Tang, W.; Bao, S.; Fang, T. Facile one-step hydrothermal synthesis of α-Fe_2O_3/g-C_3N_4 composites for the synergistic adsorption and photodegradation of dyes. *RSC Adv.* **2019**, *9*, 29109−29119.
(38) Xu, Y.; Huang, S.; Xie, M.; Li, Y.; Xu, H.; Huang, L.; Zhang, Q.; Li, H. Magnetically separable Fe_2O_3/g-C_3N_4 catalyst with enhanced photocatalytic activity. *RSC Adv.* **2015**, *5*, 95727−95735.
(39) Geng, Y.; Chen, D.; Li, N.; Xu, Q.; Li, H.; He, J.; Lu, J. Z-Scheme 2D/2D α-Fe_2O_3/g-C_3N_4 heterojunction for photocatalytic oxidation of nitric oxide. *Appl. Catal., B* **2021**, *280*, 119409.
(40) Bui, D.-P.; Nguyen, T.-D.; Le Vo, T. T.; Cao, T. M.; You, S.-J.; Pham, V. V. SnO_{2-x} Nanoparticles Decorated on Graphitic Carbon Nitride as S-Scheme Photocatalysts for Activation of Peroxymonosulfate. *ACS Appl. Nano Mater.* **2021**, *4*, 9333−9343.
(41) Bao, Y.; Song, S.; Yao, G.; Jiang, S. S-Scheme Photocatalytic Systems. *Sol. RRL* **2021**, *5*, 2100118.
(42) Xu, Q.; Zhang, L.; Cheng, B.; Fan, J.; Yu, J. S-Scheme Heterojunction Photocatalyst. *Chem* **2020**, *6*, 1543−1559.
(43) Fina, F.; Callear, S. K.; Carins, G. M.; Irvine, J. T. S. Structural Investigation of Graphitic Carbon Nitride via XRD and Neutron Diffraction. *Chem. Mater.* **2015**, *27*, 2612−2618.
(44) Gao, J.; Zhou, Y.; Li, Z.; Yan, S.; Wang, N.; Zou, Z. High-yield synthesis of millimetre-long, semiconducting carbon nitride nanotubes with intense photoluminescence emission and reproducible photoconductivity. *Nanoscale* **2012**, *4*, 3687−3692.
(45) Shi, M.; Wu, T.; Song, X.; Liu, J.; Zhao, L.; Zhang, P.; Gao, L. Active Fe_2O_3 nanoparticles encapsulated in porous g-C_3N_4/graphene sandwich-type nanosheets as a superior anode for high-performance lithium-ion batteries. *J. Mater. Chem. A* **2016**, *4*, 10666−10672.
(46) Ma, L.; Fan, H.; Fu, K.; Lei, S.; Hu, Q.; Huang, H.; He, G. Protonation of Graphitic Carbon Nitride (g-C_3N_4) for an Electrostatically Self-Assembling Carbon@g-C_3N_4 Core−Shell Nanostructure toward High Hydrogen Evolution. *ACS Sustainable Chem. Eng.* **2017**, *5*, 7093−7103.
(47) Thaweesak, S.; Wang, S.; Lyu, M.; Xiao, M.; Peerakiatkhajohn, P.; Wang, L. Boron-doped graphitic carbon nitride nanosheets for enhanced visible light photocatalytic water splitting. *Dalton Trans.* **2017**, *46*, 10714−10720.
(48) Zhao, D.; Wang, Y.; Dong, C.-L.; Huang, Y.-C.; Chen, J.; Xue, F.; Shen, S.; Guo, L. Boron-doped nitrogen-deficient carbon nitride-based Z-scheme heterostructures for photocatalytic overall water splitting. *Nat. Energy* **2021**, *6*, 388−397.
(49) Babar, S.; Gavade, N.; Shinde, H.; Gore, A.; Mahajan, P.; Lee, K. H.; Bhuse, V.; Garadkar, K. An innovative transformation of waste toner powder into magnetic g-C_3N_4-Fe_2O_3 photocatalyst: Sustainable e-waste management. *J. Environ. Chem. Eng.* **2019**, *7*, 103041.
(50) Han, T.; Wei, Y.; Jin, X.; Jiu, H.; Zhang, L.; Sun, Y.; Tian, J.; Shang, R.; Hang, D.; Zhao, R. Hydrothermal self-assembly of α-Fe_2O_3 nanorings@graphene aerogel composites for enhanced Li storage performance. *J. Mater. Sci.* **2019**, *54*, 7119−7130.
(51) Zhu, B.; Xia, P.; Li, Y.; Ho, W.; Yu, J. Fabrication and photocatalytic activity enhanced mechanism of direct Z-scheme g-C_3N_4/Ag_2WO_4 photocatalyst. *Appl. Surf. Sci.* **2017**, *391*, 175−183.
(52) Bandaru, S.; Saranya, G.; Liu, W. W.; English, N. J. First-principles studies on α-Fe_2O_3 surface slabs and mechanistic elucidation of a g-C_3N_4/α-Fe_2O_3 heterojunction. *Catal. Sci. Technol.* **2020**, *10*, 1376−1384.
(53) Meng, F.; Song, M.; Song, B.; Wei, Y.; Cao, Q.; Cao, Y. Enhanced degradation of Rhodamine B via alpha-Fe_2O_3 microspheres induced persulfate to generate reactive oxidizing species. *Chemosphere* **2020**, *243*, 125322.
(54) Li, N.; Tian, Y.; Zhao, J.; Zhang, J.; Zuo, W.; Kong, L.; Cui, H. Z-scheme 2D/3D g-C_3N_4@ZnO with enhanced photocatalytic activity for cephalexin oxidation under solar light. *Chem. Eng. J.* **2018**, *352*, 412−422.
(55) Askari, N.; Beheshti, M.; Mowla, D.; Farhadian, M. Synthesis of $CuWO_4$/Bi_2S_3 Z-scheme heterojunction with enhanced cephalexin photodegradation. *J. Photochem. Photobiol., A* **2020**, *394*, 112463.
(56) Nguyen, X. S.; Pham, T. D.; Vo, H. T.; Ngo, K. D. Photocatalytic degradation of cephalexin by g-C_3N_4/Zn doped Fe_3O_4 under visible light. *Environ. Technol.* **2021**, *42*, 1292−1301.
(57) Aram, M.; Farhadian, M.; Solaimany Nazar, A. R.; Tangestaninejad, S.; Eskandari, P.; Jeon, B.-H. Metronidazole and Cephalexin degradation by using of Urea/TiO_2/$ZnFe_2O_4$/Clinoptiloite catalyst under visible-light irradiation and ozone injection. *J. Mol. Liq.* **2020**, *304*, 112764.
(58) Rabanimehr, F.; Farhadian, M.; Nazar, A. R. S.; Moghadam, M. Fabrication of Z-scheme Bi_2WO_6/CNT/TiO_2 heterostructure with enhanced cephalexin photodegradation: Optimization and reaction mechanism. *J. Mol. Liq.* **2021**, *339*, 116728.
(59) Dou, M.; Wang, J.; Gao, B.; Xu, C.; Yang, F. Photocatalytic difference of amoxicillin and cefotaxime under visible light by mesoporous g-C_3N_4: Mechanism, degradation pathway and DFT calculation. *Chem. Eng. J.* **2020**, *383*, 123134.
(60) Chen, Q.; Chen, L.; Qi, J.; Tong, Y.; Lv, Y.; Xu, C.; Ni, J.; Liu, W. Photocatalytic degradation of amoxicillin by carbon quantum dots modified $K_2Ti_6O_{13}$ nanotubes: Effect of light wavelength. *Chin. Chem. Lett.* **2019**, *30*, 1214−1218.
(61) Nguyen, T. T.; Nam, S.-N.; Son, J.; Oh, J. Tungsten Trioxide (WO_3)-assisted Photocatalytic Degradation of Amoxicillin by Simulated Solar Irradiation. *Sci. Rep.* **2019**, *9*, 9349.